Available online at www.sciencedirect.com

ScienceDirect

Acta Materialia 86 (2015) 137–147

Acta MATERIALIA

www.elsevier.com/locate/actamat

Carbon partitioning during quenching and partitioning heat treatment accompanied by carbide precipitation

Yuki Toji,[a,*] Goro Miyamoto[b] and Dierk Raabe[c]

[a]*Steel Research Laboratory, JFE Steel Corporation, 1 Kawasaki-cho, Chuo-ku, Chiba 260-0835, Japan*
[b]*Tohoku University, 2-1-1, Katahira, Aoba-ku, Sendai 980-8577, Japan*
[c]*Max-Planck-Institut für Eisenforschung GmbH, Max-Planck-Str. 1, 40237 Düsseldorf, Germany*

Received 30 July 2014; revised 3 November 2014; accepted 27 November 2014

Abstract—Carbon partitioning from martensite into austenite in the quenching and partitioning (Q&P) process has been suggested to be controlled by the constrained carbon equilibrium (CCE) criterion. It defines an approach for predicting the carbon concentration in austenite under the condition that competing reactions such as carbide formation and bainite transformation are suppressed. Carbide precipitation in martensite is, however, often observed during the partitioning step, even in low-carbon steels as well as in high-carbon steels, even when containing a high amount of Si. Therefore, carbon partitioning from martensite into austenite is studied here, considering carbide precipitation in martensite. Carbon partitioning was investigated by means of a field-emission electron probe micro analysis (FE-EPMA) and atom probe tomography (APT), using 1.07 wt.% and 0.59 wt.% carbon steels with various martensite volume fractions. Carbon partitioning from martensite to austenite was clearly observed in all specimens, even though a considerable amount of carbide precipitated inside the martensite. The austenite carbon concentration after the partitioning step was not influenced by either the martensite volume fraction or the bulk carbon content. A modified model for predicting the austenite carbon concentration after the partitioning step was proposed to explain the experimental results by assuming carbon equilibria between austenite, ferrite and cementite under a constrained condition.

Keywords: Quenching and partitioning; Carbide; Cementite; EPMA; Atom probe tomography

1. Introduction

Quenching and partitioning (Q&P) steels yield an excellent balance of high tensile strength and good elongation, with chemical compositions similar to conventional TRIP steels [1–4]. They are produced via the Q&P process, which consists of a quenching and a following partitioning step. During the quenching step, fully austenitized or intercritically annealed steels are quenched to temperatures (hereafter referred to as "quench temperature") below the martensite start (M_s) temperature, but above the martensite finish (M_f) temperature in order to form a controlled volume fraction of martensite. The quenched steels are then held at temperatures the same as or higher than the quench temperature during the subsequent partitioning step. Austenite that prevails after quenching is considered to be stabilized through carbon partitioning from martensite into austenite during the partitioning treatment.

It has been suggested that the carbon partitioning from martensite into austenite is controlled by the constrained carbon equilibrium (CCE) criterion [5]. This criterion aims to predict the carbon concentration in austenite under the condition where: (i) competing reactions, such as cementite or transition carbide formation or bainite transformation, are suppressed; (ii) an identical carbon chemical potential exists in both ferrite (or martensite) and austenite; and (iii) the carbon partitioning proceeds under the assumption that the interface between ferrite and austenite does not migrate. However, carbide precipitation in martensite is often observed during the partitioning step, even in low-carbon steels [6] as well as in high-carbon steels [7,8], even if they contain a high amount of Si [9]. If carbide precipitates, some of the carbon is consumed to form the carbide, reducing the remaining amount of carbon in martensite that can be enriched in austenite during partitioning. Hence, the austenite carbon concentration after the partitioning step in this case is presumed to be lower than that predicted under the CCE conditions excluding carbide precipitation. As Speer et al. [1] pointed out, it is important to choose appropriate chemical compositions in order to avoid carbide precipitation in realizing an ideal Q&P condition. However, as some carbide formation may always occur, adequate models are required that describe such a case, thus providing a more precise estimate of the carbon concentration in austenite after the Q&P heat treatment. There is, however, currently no model dealing with the

* Corresponding author. Tel.: +81 44 322 6126; e-mail: y-toji@jfe-steel.co.jp

http://dx.doi.org/10.1016/j.actamat.2014.11.049
1359-6462/

carbon partitioning behavior from martensite into austenite under conditions in which carbide precipitation occurs in martensite during the partitioning step.

Therefore, this study conducts an experimental analysis of the carbon partitioning behavior from martensite into austenite accompanied by carbide precipitation inside the martensite during a partitioning step. A modified CCE model is introduced to explain the experimental results.

2. Experimental procedure

The chemical compositions of the steels used in this study are listed in Table 1. The carbon contents in these model alloys were higher than that in typical alloys used for Q&P processing [1,10] in order to lower the M_f temperature below room temperature. For these alloys, room temperature or even lower temperatures can be used as the quench temperature, which enables direct observation of the initial microstructure and atomic distribution before the partitioning step. The high amount of Si (~2 wt.%) was added to suppress carbide formation [9]. The steels were prepared by vacuum induction melting. The ingots were homogenized at 1240 °C for 48 h and then air cooled to room temperature. The homogenized ingots were reheated and held at 1200 °C for 30 min, followed by hot rolling to sheets with thickness 3.6 mm, and finally air cooled to room temperature. Specimens with dimensions 15 × 50 mm, cut from the hot-rolled sheets, were then heat-treated according to Fig. 1. They were austenitized at 900 °C for 3 min, then quenched in water at a temperature of 30–17 °C, followed by a partitioning step at 400 °C for 300 s in a salt bath furnace. Some specimens cut from steel A (see Table 1) quenched in 17 °C water were further quenched to −20 °C or −63 °C prior to the partitioning step to vary the martensite volume fraction. The specimens before and after the partitioning step are hereafter referred to as "as-quenched specimen" and "partitioned specimen", respectively. Although slight decarburization occurred near the surface during homogenization and reheating, it was confirmed that the carbon concentration at least at one-quarter of the thickness of the heat-treated sheets was identical to the bulk carbon concentration. Therefore, all the following characterization steps were performed at one-quarter of the thickness of the heat-treated sheets to avoid the decarburized layer.

Table 1. Chemical compositions of steels used (wt.%).

Steel	C	Si	Mn	Al	Fe
A	1.07	2.2	2.9	0.048	Bal.
B	0.59	2.0	2.9	0.038	Bal.

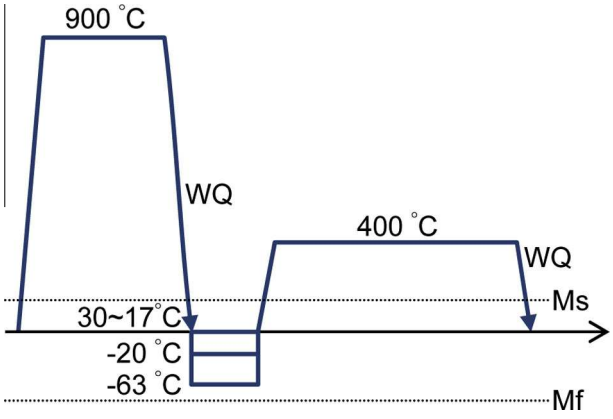

Fig. 1. Schematic diagram of heat treatment: M_s, martensite start temperature; M_f, martensite finish temperature; WQ, water-quenching.

Microstructures in the cross section perpendicular to the transverse direction (TD cross section) etched with 0.1–0.3% Nital were observed by optical microscopy and scanning electron microscopy (SEM). The austenite volume fraction change during the partitioning step was investigated by X-ray diffraction (XRD) with Co K_α radiation, using the intensities of the (200)α, (211)α, (200)γ, (220)γ and (311)γ reflections. The samples for XRD analysis were ground from the surface to one-quarter of the thickness of the heat-treated steels and, subsequently, another 100 μm was removed from the ground surface by means of electrolytic polishing to exclude any influence of strains that might have been introduced by the grinding step.

Carbon partitioning between martensite and austenite was investigated mainly using a field-emission electron probe micro analysis (FE-EPMA) [11]. The use of a FE-type electron emitter can achieve a narrower emission area compared with the conventional W or LaB_6-type electron emitter. Also, a relatively low voltage of 6 kV was used to minimize the excitation volume. A probe current of 70 nA was used. The carbon concentration was determined using a standard calibration curve, which was obtained using seven standard specimens in the range 0.0083–1.07 wt.% C (Fig. 2). Standard deviations for each plot in Fig. 2 are expressed as error bars, which are <0.021 wt.%. In the FE-EPMA measurements, the line-analysis mode is used to obtain carbon profiles across regions of interest. The detection time for each point was 2 s in single-scan mode.

Atom probe tomography (APT) [12–21] was used for the atomic scale quantitative investigation of elemental partitioning during the partitioning step. Samples for APT measurements were prepared using focused ion beam milling and the lift-out procedure described in Ref. [22]. APT analyses were performed using a local electrode atom probe (LEAP 3000X HR, Cameca Instruments) in voltage mode at a specimen temperature of ~65 K. The pulse fraction and the pulse rate were 15% and 200 kHz, respectively.

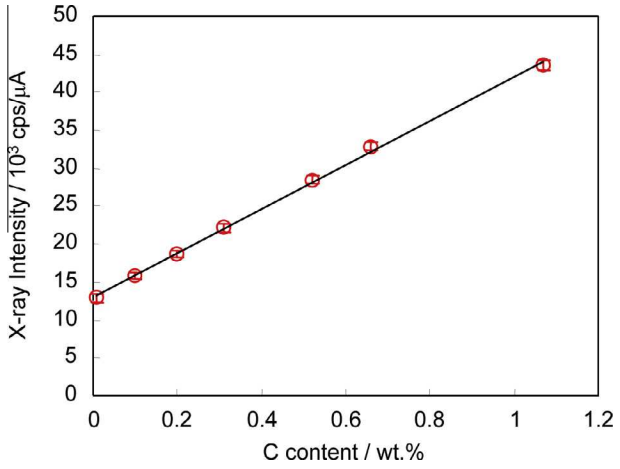

Fig. 2. Standard calibration line for FE-EPMA measurements. The error bars represent standard deviation.

Data analysis was performed using the IVAS software (Cameca Instruments). The acquired mass spectra revealed peaks corresponding to C^+, C^{2+}, C_2^+, C_3^+, C_3^{2+}, C_4^{2+}, Fe^{2+}, Si^{2+}, Mn^{2+}, Al^{2+} and Al^{3+}. In most analyses, the $(^{12}C_3^{13}C)^{2+}$ peak at a mass-to-charge ratio (Da) of 24.5 was detected. This means that the peak at 24 Da, 25 Da and 26 Da could be due to either C_2^+ or C_4^{2+}, or a mixture of both [23,24]. Therefore, a peak decomposition algorithm supplied by the IVAS software was applied to decompose these peaks.

3. Results

3.1. Influence of martensite volume fraction on carbon partitioning behavior

Fig. 3 shows optical micrographs of steel A (1.07 wt.% C; see Table 1) quenched to (a) 30 °C, (b) 17 °C, (c) −20 °C and (d) −63 °C, respectively, followed by a partitioning step at 400 °C for 300 s. The dark regions are martensite, which forms during quenching, and the white regions are austenite. The volume fraction of martensite increased with decreasing quench temperature: namely, 15% (quenched to 30 °C), 22% (quenched to 17 °C), 52% (quenched to −20 °C) and 75% (quenched to −63 °C), respectively. Fig. 4a and b shows SEM images of the specimens as-quenched to 17 °C, while Fig. 4c–h corresponds to the specimens partitioned at 400 °C for 300 s after quenching to (c, d) 30 °C, (e, f) 17 °C and (g, h) −63 °C. No carbide was observed in the as-quenched specimen (Fig. 4a, b). In contrast, a considerable amount of carbide (white contrast) can be observed inside the martensite in the partitioned specimens (Fig. 4c–h). The number density of the carbide in the specimen quenched to 30 °C (Fig. 4c, d) seems to be slightly lower compared with that in the specimens quenched to 17 °C and −63 °C (Fig. 4e–h). Lines with higher carbide number density indicated by white arrows can be seen inside the martensite plates, which correspond to the midribs of the lenticular martensite [25]. No further structural feature, such as bainite, was observed under the present experimental conditions. Fig. 5 shows the austenite volume fraction change by holding at 400 °C of the specimens quenched to several temperatures (17 to −63 °C). The specimens were heat treated at 400 °C for 10–3000 s, followed by quenching to room temperature. The austenite volume fraction in each specimen was measured by means of XRD. There is essentially no change in austenite volume fraction up to 3000 s. This indicates that austenite decomposition, i.e. bainite transformation, did not occur under the partitioning conditions in this study.

Carbon partitioning during the partitioning step in the specimens with different martensite volume fraction was investigated by means of FE-EPMA. At first, the carbon distributions in the specimens as-quenched to 17 °C and −63 °C with different martensite volume fractions (22% and 75%, respectively) are shown in Fig. 6. These two cases are taken as upper and lower bounds, respectively. Line probes with 20 μm analysis length were performed in regions containing both martensite and austenite. In the as-quenched specimens, the carbon distributions were almost uniform within the experimental error, irrespective of the martensite volume fraction. No substantial difference in carbon level and scatter is observed between these two specimens. This observation indicates that the carbon partitioning from martensite to austenite during quenching to each of these temperatures was essentially negligible, which is in line with previous results obtained on steel B (0.59 wt.% C; see Table 1) via APT [8]. The averaged carbon concentration value in these two specimens, as obtained by FE-EPMA, was ~1.087 wt.%, which is close to the bulk carbon content of the material (1.07 wt.%; Table 1).

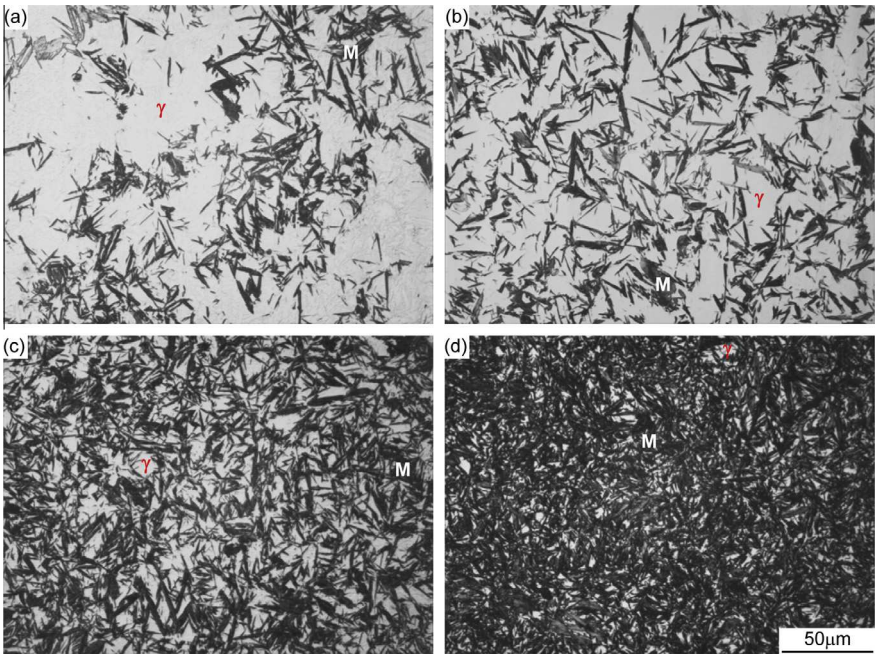

Fig. 3. Optical micrographs of steel A (1.07 wt.% C; see Table 1) quenched to (a) 30 °C, (b) 17 °C, (c) −20 °C and (d) −63 °C, followed by partitioning at 400 °C for 300 s. γ, austenite; M, martensite.

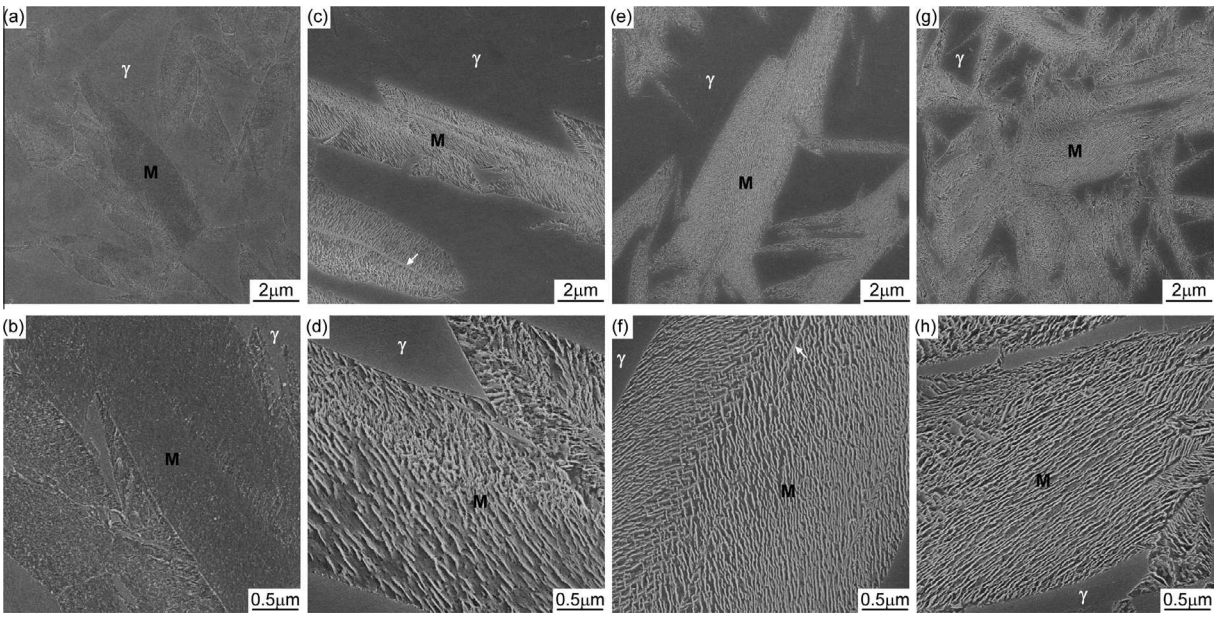

Fig. 4. SEM micrographs of steel A (1.07 wt.% C; see Table 1): (a, b) as-quenched to 17 °C, (c, d) quenched to 30 °C followed by partitioning at 400 °C for 300 s; (e, f) quenched to 17 °C followed by partitioning at 400 °C for 300 s, (g, h) quenched to −63 °C followed by partitioning at 400 °C for 300 s. Arrows indicate midribs in martensite. γ austenite; M, martensite.

Fig. 7 shows FE-EPMA carbon profiles of the specimens quenched to 17 °C and −63 °C, respectively, followed by partitioning at 400 °C for 300 s. Note that the magnification of the two SEM images is different, and the size of the austenite regions in Fig. 7b is smaller than that in Fig. 7a. The white lines in the upper SEM images indicate the probed lines. Compared with the as-quenched specimens shown in Fig. 6, the carbon distribution in these partitioned specimens is obviously inhomogeneous. Clear pileup of carbon around the martensite/austenite (M/A) interface inside the austenite region can be observed (blue arrows in Fig. 7c, d). This indicates that some carbon atoms could partition from the martensite into the austenite during the partitioning step at 400 °C, even though a considerable amount of carbide formed inside the martensite. Regarding the carbon concentration in the martensite, it should be noted that it is the averaged value of both ferrite and carbide in martensite, because the carbide size is too small relative to the resolution of the FE-EPMA. Therefore, if the carbide number density is locally high (e.g. at the midribs inside the martensite; see Fig. 4), the detected carbon concentration is higher, as indicated by the red arrow in Fig. 7c.

The austenite carbon concentration in the specimens partitioned at 400 °C for 300 s obtained by FE-EPMA is summarized in Fig. 8 as a function of the martensite volume fraction. Although the carbon concentration was not homogeneous in the austenite after partitioning for 300 s, as shown in Fig. 7, the austenite carbon concentration in the vicinity of the M/A interface is the most important information to understand the equilibrium conditions across the interface. Therefore, the range of the austenite

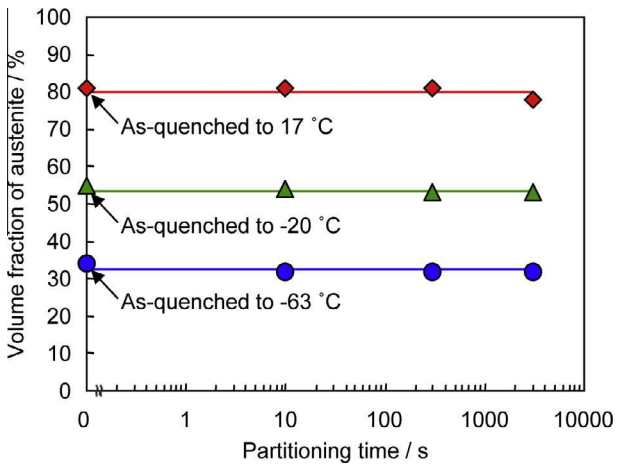

Fig. 5. Austenite volume fraction change by partitioning at 400 °C obtained by XRD.

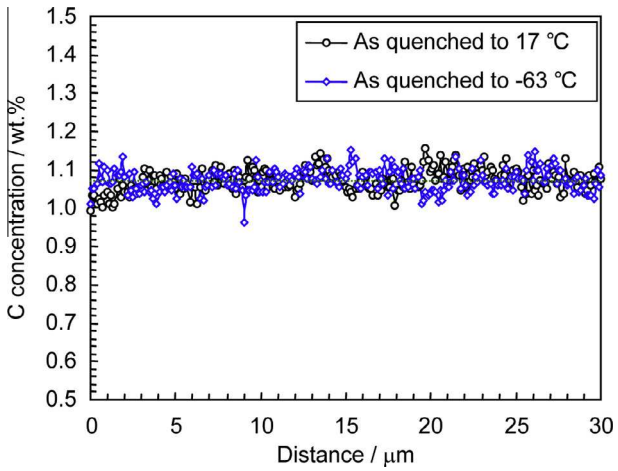

Fig. 6. Carbon concentration profiles of steel A (1.07 wt.% C; see Table 1) as-quenched to 17 °C and −63 °C obtained by FE-EPMA.

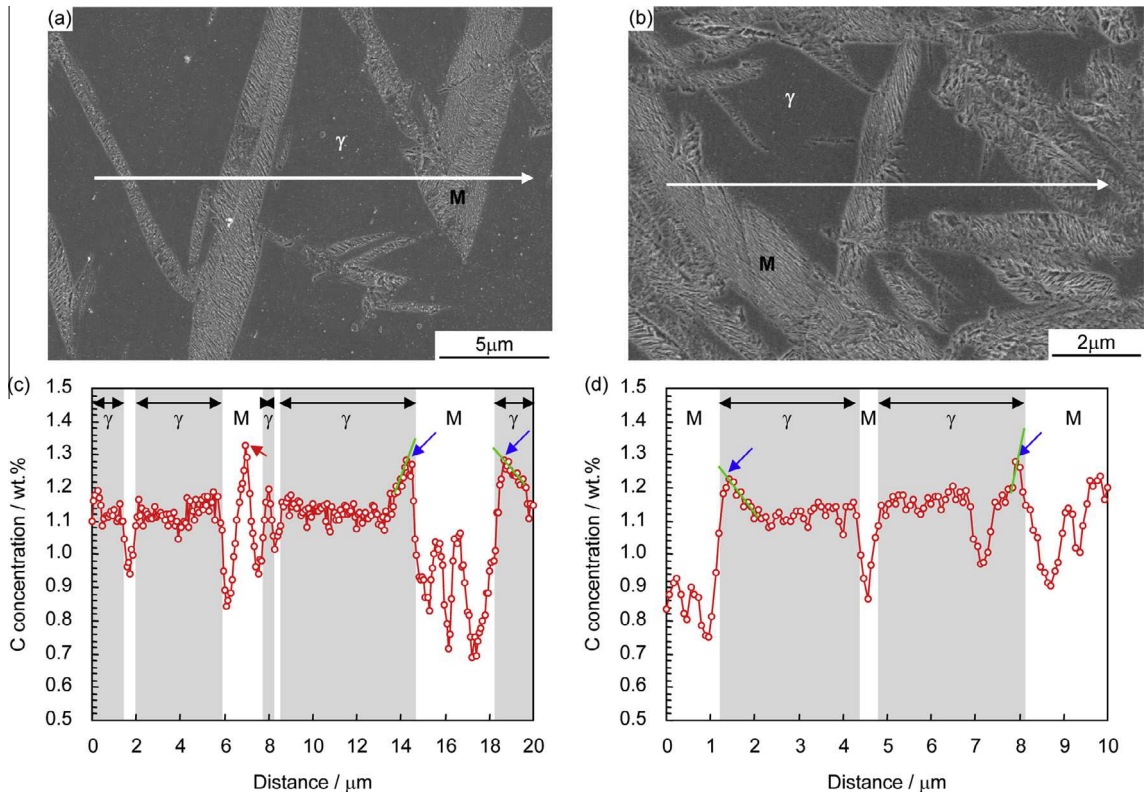

Fig. 7. SEM microstructures of steel A (1.07 wt.% C; see Table 1) quenched to (a) 17 °C and (b) −63 °C followed by partitioning at 400 °C for 300 s. Carbon concentration profiles along the white arrows in (a) and (b) obtained by FE-EPMA are shown in (c) and (d), respectively. Blue arrows in (c) and (d) indicate the pile up of carbon in austenite in the vicinity of the interface. Red arrow indicates a midrib of a martensite. γ, austenite; M, martensite. (For interpretation of the references to colour in this figure legend, the reader is referred to the web version of this article.)

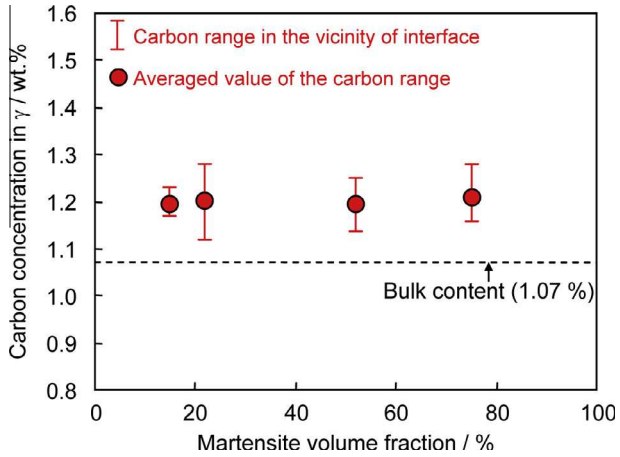

Fig. 8. Influence of martensite volume fraction on austenite carbon concentration in steel A (1.07 wt.% C, see Table 1) quenched to 30 to −63 °C followed by partitioning at 400 °C for 300 s. γ, austenite.

carbon concentration values in the vicinity of the M/A interfaces is shown as red bars in Fig. 8. In either specimen with their different martensite fractions, the austenite carbon concentrations are higher than the bulk carbon content (1.07 wt.%). The most important finding here is that the austenite carbon concentration near the interface in these specimens with different martensite volume fraction is nearly the same. This indicates that the carbon partitioning behavior is not influenced by the volume fraction of pre-existing martensite.

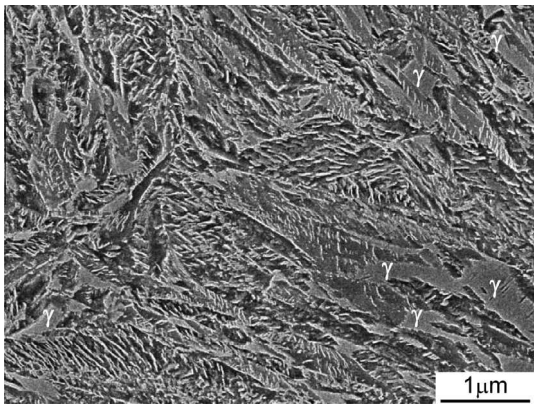

Fig. 9. SEM microstructure of steel B (0.59 wt.% C; see Table 1) partitioned at 400 °C for 300 s after quenching to 17 °C. γ, austenite.

3.2. Influence of bulk carbon content on carbon partitioning behavior

In order to understand the influence of the bulk carbon concentration on carbon partitioning behavior, carbon partitioning in the lower-carbon steel (steel B, 0.59 wt.% C; Table 1) was also investigated. The contents of the other alloying element (Si, Mn, Al) in steel B are nearly the same as those in steel A (1.07 wt.% C). Fig. 9 shows the SEM micrograph of steel B quenched to room temperature (17 °C) followed by partitioning at 400 °C for 300 s. Many plate-shaped carbides with white contrast are observed in

the martensite. The larger regions appearing in gray contrast are retained austenite with a volume fraction of 8%, as measured by XRD [8]. It was confirmed by means of dilatometry and XRD probing that no bainite transformation occurred during the partitioning step [8].

For the investigation of carbon partitioning in this specimen, APT was applied, since the spatial resolution of FE-EPMA (estimated as ~0.3 μm under the measurement conditions used here) is not fine enough relative to the size of the austenite regions in this specimen. Fig. 10 shows a carbon atom map of the specimen partitioned at 400 °C for 300 s, and a concentration profile (here converted from at.% into wt.% to render it comparable with the data shown in Fig. 7) along the arrow indicated in the carbon atom map. The yellow envelopes in the carbon atom map are the iso-concentration surfaces representing 0.59 wt.% carbon, which is the bulk carbon content of this steel. Carbon enrichment in the austenite can be clearly observed. It was confirmed by APT that the carbon partitioning from martensite to austenite during water-quenching and sample storage at room temperature was essentially negligible, and the average carbon concentration obtained from eight as-quenched samples analyzed by APT was 0.62 wt.% (2.77 at.%) [8]. This value is in good agreement with the bulk carbon content of the steel (0.59 wt.%). Therefore, it is concluded that the observed carbon enrichment in the austenite was caused by carbon partitioning from martensite to austenite during the partitioning step. The carbon concentration inside the austenite was ~1.2 wt.%, which is about twice as high as the bulk carbon concentration. The accurate austenite carbon concentrations were analyzed inside the austenite regions at least 2 nm away from the interface between martensite and austenite in order to exclude the influence of the artifact around the interface (i.e. the local magnification effect which may artificially broaden the interface). The interface was defined as the median of the carbon concentration gradient between the two phases. The averaged carbon concentration obtained from the austenite regions in five atom probe samples were 1.41 wt.% (6.11 at.%). This value is similar to or slightly higher than the austenite carbon concentrations observed in the 1.07 wt.% C steel (steel A, Table 1) shown in Fig. 7, even though the bulk carbon concentration of steel B is lower than that of steel A.

4. Discussion

4.1. Comparison between experimental results and the CCE model

In this section, the experimentally observed carbon partitioning behavior is compared with the CCE model proposed by Speer et al. [5]. Fig. 11 shows the experimentally obtained carbon concentrations in austenite, together with the values predicted by the CCE model. Regarding the

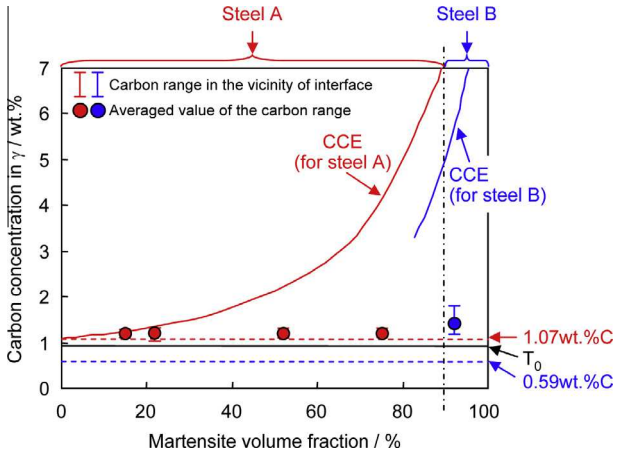

Fig. 11. Comparison between the experimentally obtained carbon concentrations in austenite and that predicted by CCE model. Note that the specimen with 92% martensite is steel B. The bulk carbon content of steel A is 1.07 wt.% and that of steel B is 0.59 wt.%, indicated as red and blue broken lines. T_0 represents the carbon concentration where free energies in ferrite and austenite are identical. γ, austenite. (For interpretation of the references to colour in this figure legend, the reader is referred to the web version of this article.)

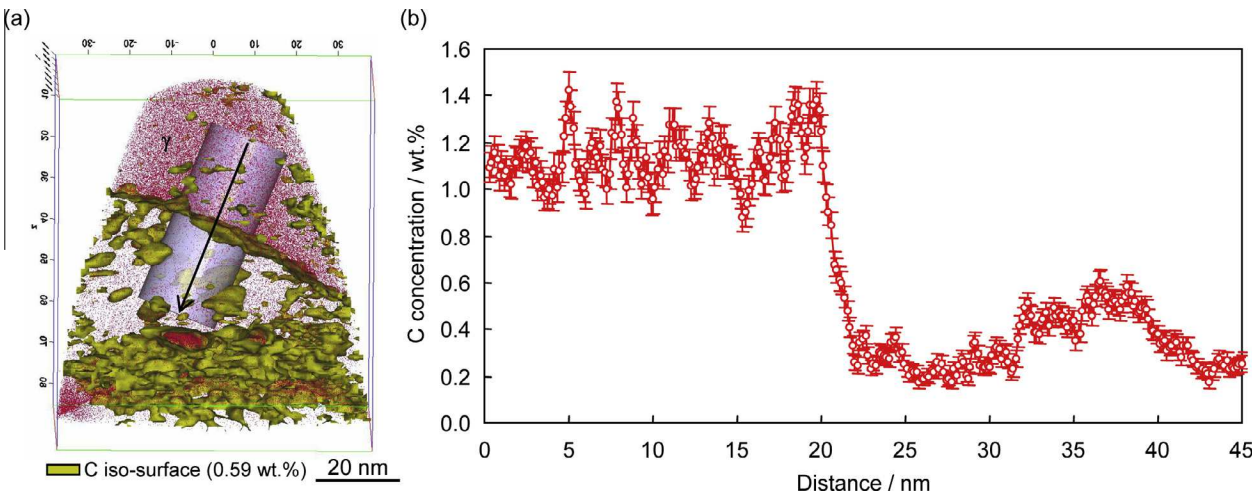

Fig. 10. (a) Carbon atom map of steel B (0.59 wt.% C; see Table 1) partitioned at 400 °C for 300 s. (b) Carbon concentration profile along the arrow indicated in the carbon atom map (a). The yellow surfaces in (a) are iso-concentration surfaces with 0.59 wt.% C. The error bars in (b) represent the one-sigma statistical error. γ, austenite. (For interpretation of the references to colour in this figure legend, the reader is referred to the web version of this article.)

experimental data, the austenite carbon concentrations in the 1.07 wt.% C steel (steel A, Table 1) with a martensite volume fraction of 15–75% (corresponding to the different quench temperatures; Fig. 3) and those in the 0.59 wt.% C steel (steel B) with 92 vol.% martensite are plotted together. The range of the austenite carbon concentration values in the vicinity of the M/A interface and their averaged values are shown in this figure. As mentioned before, the martensite volume fraction has essentially no influence on the experimentally obtained austenite carbon concentrations in steel A. In addition to that, the austenite carbon concentration in steel B is also nearly the same as those in steel A, although that in steel B is slightly higher than those in steel A. This small difference in the austenite carbon concentration between these two steels is attributed to the different analysis techniques (FE-EPMA in the case of steel A; APT in the case of steel B). The carbon values obtained by FE-EPMA cannot reveal the real austenite carbon concentration in the vicinity of the M/A interface, owing to its limited spatial resolution. If the slope of the carbon concentration profile near the interface in Fig. 7 is extrapolated to the interface, the value approaches 1.3–1.4 wt.% (see green lines near the interface in Fig. 7c, d), which is closer to the austenite carbon concentration in the vicinity of the interface in steel B analyzed by APT. Therefore, it is concluded that the austenite carbon concentration in the vicinity of the interface was not influenced either by the martensite volume faction or by the bulk carbon concentration of the alloys. It should also be noted that the experimentally obtained carbon concentration in the austenite is higher than the carbon concentration at point T_0 at 400 °C (shown as a black line in Fig. 11) where the free energies of the ferrite and the austenite phases are identical. For the case of the displacive mechanism, the bainite transformation is considered to stop when the austenite carbon concentration reaches T_0 (or T'_0 ($<T_0$), when accounting for the stored energy of bainite) [26], because there is no driving force for the transformation from face-centered cubic to body-centered cubic without carbon diffusion if the austenite carbon concentration is $>T_0$. This also indirectly proves that the carbon enrichment in austenite observed in this study is not caused by the bainite transformation, but by carbon partitioning from martensite.

The austenite carbon concentration predicted by the CCE model is drawn as the red and blue solid lines for steel A and steel B, respectively. The values were calculated in the same way as reported in Ref. [8]. According to the CCE model, the carbon concentration in austenite is predicted to increase with increasing martensite volume fraction and bulk carbon content [5]. Therefore, more carbon can accumulate inside the austenite if the martensite volume fraction is larger and the austenite volume fraction is smaller. Regarding the influence of the bulk carbon content, more carbon can enrich in austenite in steels with higher bulk carbon content compared with the steels with lower bulk carbon content having same martensite volume fraction. It should be noted that the CCE theory predicts the austenite carbon concentration at the end-point (i.e. when carbon partitioning has finished) [5]. However, the partitioning condition in this study (400 °C for 300 s) does not seem to be the end-point, since there is a gradient of the carbon concentration near the M/A interface (Fig. 7). Under CCE conditions, the austenite carbon concentration at the interface is predicted to decrease with increasing partitioning time owing to the slower carbon diffusion in austenite than that in ferrite [27]. Therefore, even though the carbon partitioning has not finished, the austenite carbon concentration at the interface should have some relationship with the martensite volume fraction under CCE conditions, since it must always be above the carbon concentration at the end-point shown as red and blue lines in Fig. 11, regardless of the martensite volume fraction.

This tendency predicted by the CCE model is, however, inconsistent with the experimental results obtained in the present study with different martensite volume fractions and bulk carbon contents under the conditions that carbide precipitates in martensite. This deviation is attributed to the carbide precipitation inside the martensite, as observed in this study (Fig. 4), which is not considered in the CCE model. Carbide precipitation consumes some of the carbon, thus its partitioning into austenite is reduced. Hence, a modified model is suggested in the ensuing section to

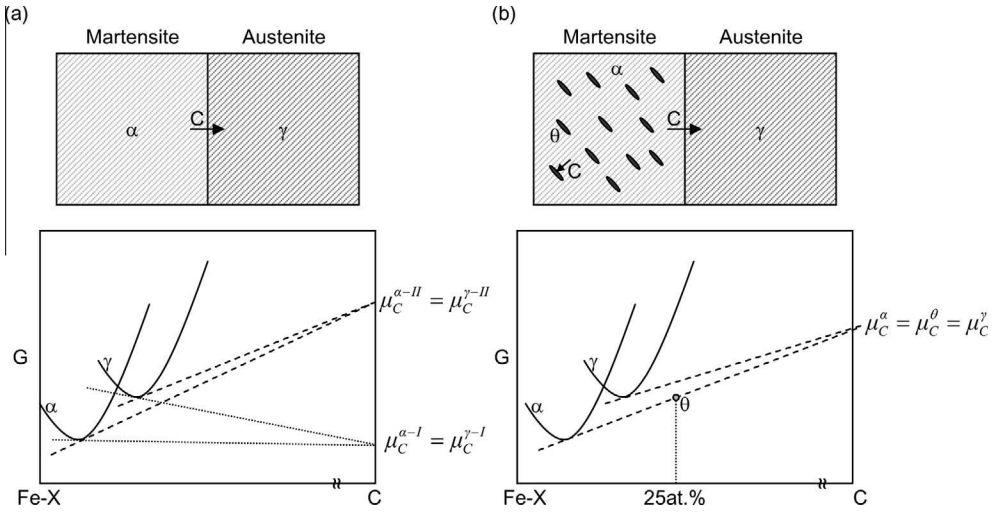

Fig. 12. Comparison between (a) original CCE model and (b) modified CCE model: α, ferrite; γ, austenite; θ, cementite; C, carbon; Fe, iron; X, substitutional elements; μ_C^{α}, μ_C^{γ}, μ_C^{θ}, carbon potential in ferrite, austenite and cementite, respectively.

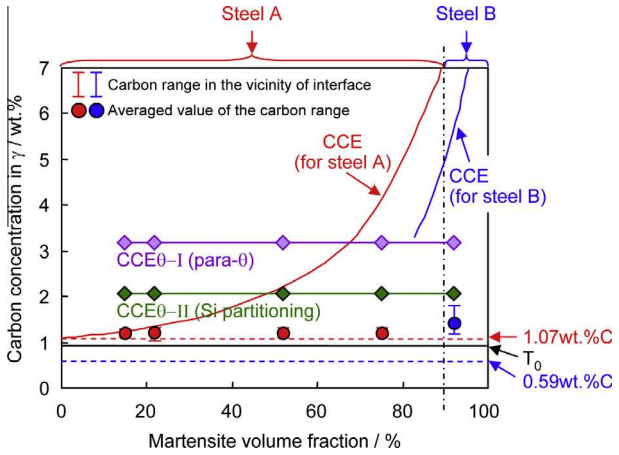

Fig. 13. Comparison between the experimentally obtained carbon concentrations in austenite and that predicted by CCEθ (CCE accompanied by θ precipitation) model. CCEθ-I assumes para-θ precipitation and CCEθ-II assumes Si partitioning between θ and surrounding ferrite at 400 °C for 300 s. Carbon concentrations in austenite predicted by CCE for steel A and steel B are also drawn. Note that the specimen with 92% martensite is steel B. The bulk carbon content of steel A is 1.07 wt.% and that of steel B is 0.59 wt.%, indicated as red and blue broken lines. T_0 represents the carbon concentration where free energies in ferrite and austenite are identical. γ, austenite. (For interpretation of the references to colour in this figure legend, the reader is referred to the web version of this article.)

understand the carbon partitioning behavior under consideration of carbide precipitation in martensite.

4.2. Modified carbon partitioning model including carbide precipitation

Here, a modified CCE model is proposed to understand the carbon partitioning behavior in the case where carbide precipitation occurs in martensite. The modified CCE model, hereafter referred to as CCEθ (constrained carbon equilibrium accompanied by θ precipitation) is drawn schematically in Fig. 12, together with the original CCE model. Fe–X on the left-hand side of the abscissa refers to iron (Fe) with other substitutional elements (X) included in alloys. The atomic fraction of substitutional elements such as Si, Mn is constant in these diagrams. In the original CCE model, carbide precipitation is not taken into account, i.e. only carbon partitioning between martensite (ferrite) and austenite is considered.

In the model proposed here, the free energy of the cementite is also drawn (Fig. 12b). The cementite is generally treated as a stoichiometric compound containing 25 at.% C even though the carbon concentration can vary slightly to values <25 at.% in cementite [28–30]. Therefore, the free energy of cementite in the Fe–X–C diagram is here represented as a dot. Since the cementite precipitates inside the martensite, the carbon potential in the ferrite and cementite in the martensite should be identical. In addition, the carbon potential in the austenite should be the same as that in ferrite, which is satisfied by drawing a tangent to the austenite free energy curve from the point where the tangent to the ferrite free energy curve intersects the carbon axis (right axis). This condition is expressed by the following equations:

$$3\mu^{\alpha}_{Fe_{CCE\theta}} + \mu^{\alpha}_{C_{CCE\theta}} = G(Fe_3C) \quad (1)$$

$$\mu^{\alpha}_{C_{CCE\theta}} = \mu^{\gamma}_{C_{CCE\theta}} \quad (2)$$

where $\mu^{\alpha}_{Fe_{CCE\theta}}$ is the chemical potential of iron in ferrite, $\mu^{\alpha}_{C_{CCE\theta}}$ and $\mu^{\gamma}_{C_{CCE\theta}}$ are the chemical potentials of carbon in ferrite and austenite under CCEθ conditions, respectively. $G(Fe_3C)$ is the Gibbs free energy of cementite. Eq. (1) expresses the tangent to the ferrite free energy curve passing the point of the cementite free energy. These conditions are coupled with the condition that the interface between ferrite and austenite does not migrate, which is expressed as the following form:

$$f^{\gamma}_{CCE\theta}(1 - X^{\gamma}_{C_{CCE\theta}}) = f^{\gamma}_{i}(1 - X^{alloy}_{C}) \quad (3)$$

where f^{γ}_{i} and $f^{\gamma}_{CCE\theta}$ represent the initial austenite mole fraction before the partitioning step and the austenite mole fraction under CCEθ conditions, respectively. X^{alloy}_{C} and $X^{\gamma}_{C_{CCE\theta}}$ represent the bulk carbon concentration, and the carbon concentration in the austenite under CCEθ conditions, respectively. This equation means that the atomic fractions of the substitutional elements in the austenite do not change during the partitioning step. The following two more equations are required to describe the carbon equilibria.

$$f^{\alpha}_{CCE\theta}X^{\alpha}_{C_{CCE\theta}} + f^{\gamma}_{CCE\theta}X^{\gamma}_{C_{CCE\theta}} + f^{\theta}_{CCE\theta}X^{\theta}_{C_{CCE\theta}} = X^{alloy}_{C} \quad (4)$$

$$f^{\alpha}_{CCE\theta} + f^{\gamma}_{CCE\theta} + f^{\theta}_{CCE\theta} = 1 \quad (5)$$

where $f^{\alpha}_{CCE\theta}$ and $f^{\theta}_{CCE\theta}$ represent the ferrite and cementite mole fractions under CCEθ conditions, respectively. $X^{\alpha}_{C_{CCE\theta}}$ and $X^{\theta}_{C_{CCE\theta}}$ represent the carbon concentrations in ferrite and cementite under CCEθ conditions, respectively ($X^{\theta}_{C_{CCE\theta}} = 0.25$). Eq. (4) expresses the mass balance of carbon. Eq. (5) describes the relationship among the phase fractions. The situation expressed by Fig. 12 and Eqs. (1–5) is that (i) the ferrite and cementite are under para equilibrium conditions, and (ii) the ferrite (which contains cementite) and the abutting austenite are under CCE conditions. This means that the austenite volume fraction does practically not change, while the ferrite volume fraction changes accompanied by the cementite precipitation. In reality, the austenite volume fraction should, of course, change slightly as the atomic fraction of carbon inside the austenite increases during the partitioning step.

An essential difference between the CCE and CCEθ models is the influence of the initial austenite volume fraction and the carbon content before the partitioning step on the resultant austenite carbon concentration after partitioning. Under CCE conditions at a specific partitioning temperature, there is an infinite set of carbon concentrations in ferrite and austenite with equal carbon potentials as shown in Fig. 11a. Hence, the initial austenite fraction and carbon content is required to select one of them [5]. In other words, the austenite carbon concentration changes with the initial austenite fraction and carbon content. However, it is expected that the austenite carbon concentration is uniquely identified only by the thermodynamic conditions as shown in Fig. 12b under CCEθ conditions, independent of the initial austenite volume fraction and carbon content if the contents of other alloying elements such as Si and Mn in the alloys are the same. In this case, the volume fraction of carbide inside the martensite would change as a function of the initial martensite fraction and bulk carbon content, so as to provide the required carbon

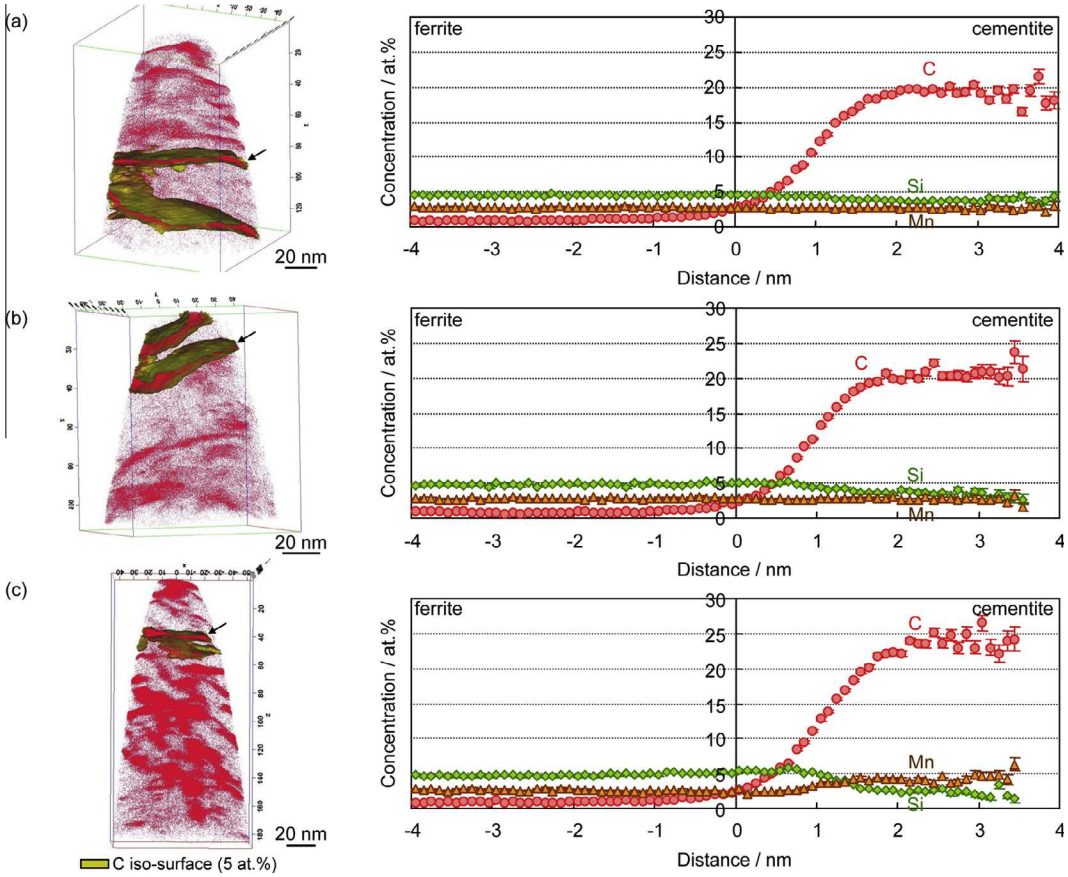

Fig. 14. Carbon atom maps of steel B (0.59 wt.% C; see Table 1) partitioned at 400 °C for (a) 10 s, (b) 300 s and (c) 3000 s, and average compositions of C, Si, Mn relative to the position of the 5 at.% C iso-surface around the carbides indicated by the arrows in the carbon atom maps. The yellow surfaces in the carbon atom maps are iso-concentration surfaces with 5 at.% C. The error bars in concentration profiles represent the one-sigma statistical error.

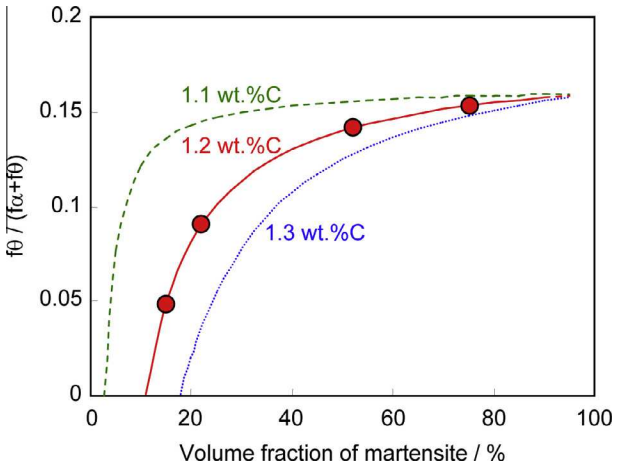

Fig. 15. Cementite fraction in martensite of steel A (1.07 wt.% C; see Table 1) at 400 °C as a function of martensite volume fraction. Austenite carbon concentration is assumed to be 1.1–1.3 wt.%. θ, cementite; α, ferrite. (fα + fθ) represents volume fraction of martensite.

atoms to maintain the identical austenite carbon concentration, which will be discussed in Section 4.3.

The CCEθ approach is also different from ortho- and para-equilibrium conditions. Under these equilibrium conditions, carbon never partitions to austenite without accompanying austenite-to-ferrite transformation.

4.3. Comparison between experimental results and the modified carbon partitioning model

The austenite carbon concentrations as predicted by the CCEθ model under the two cases are drawn as purple and green lines in Fig. 13, together with the experimental data. The free energies of austenite, ferrite and cementite at 400 °C were calculated by Thermo-Calc using the TCFE6 database. CCEθ-I (purple line) assumes that the carbides observed in this study were para-cementite, which means that the substitutional atomic fractions of Si and Mn in the cementite are identical to those in ferrite and austenite. This is considered to be the initial state of the carbide precipitation [31].

As discussed in Section 4.1, the partitioning condition in this study (400 °C for 300 s) does not seem to be the end-point of the carbon partitioning process. Even though the carbon partitioning has not finished, one can discuss the equilibrium conditions according to the CCEθ model using the austenite carbon concentration at the interface for the following reason. In the case of the CCEθ model, once carbide precipitates in martensite, the carbon chemical potential in ferrite is fixed to the same value as that in cementite. Some carbon atoms promptly partition from martensite to

austenite in order to maintain the continuity of the carbon potential in the entire system, i.e. the carbon potential in austenite at the interface becomes identical to that in ferrite. If it is assumed that the carbon potential in cementite does not change during the partitioning step, the carbon potential in ferrite and in austenite at their interface should not change either. Therefore, the austenite carbon concentration at the interface does not change during the partitioning step, which is different from the situation assumed under the original CCE conditions.

According to the CCEθ prediction, the austenite carbon concentration is neither influenced by the initial austenite volume fraction nor by the nominal carbon content as mentioned above. Therefore, the purple line is horizontal, regardless of the martensite volume fraction and the bulk carbon content. This is consistent with the trend observed in the experimental results, which supports the applicability of the CCEθ model for predicting the carbon concentration in austenite in cases when carbides precipitate inside the martensite.

However, the austenite carbon concentration calculated by the CCEθ model (CCEθ-I) is relatively higher than the experimental values. This can probably be attributed to the fact that the free energy of cementite is not entirely correct. If substitutional elements such as Mn, Si partition between ferrite and cementite, the free energy of cementite is reduced [31,32]. This decreases the carbon potential in ferrite in equilibrium with the cementite, and hence also lowers the carbon potential in austenite. As a result, the austenite carbon concentration under CCEθ conditions should shift to lower values. In order to modify the calculation conditions closer to the actual experimental situation, the partitioning of the substitutional elements between ferrite and cementite were investigated by means of APT. Fig. 14 shows carbon atom maps obtained for steel B (0.59 wt.% C; Table 1) partitioned at 400 °C for 10–3000 s, together with the corresponding proximity histograms (proxigrams) [33] across the 5 at.% carbon iso-surfaces indicated by the arrows. The carbon concentration inside the carbon enriched regions is nearly 25 at.%, matching the stoichiometric carbon concentration in cementite. Thus, these carbon enriched regions are identified as cementite. Si partitioned only slightly after 10 s. However, the partitioning of Si and Mn proceeds with increasing partitioning time. After 300 s, which corresponds to the partitioning condition discussed in Fig. 13, Mn did still not partition substantially. In contrast, Si partitioning is relatively obvious, and the difference in Si concentration between the ferrite and cementite regions in this case is ~2.3 at.%. The cementite free energy change caused by this degree of Si partitioning was calculated by Thermo-Calc (TCFE6). The decrement in the cementite free energy was 1760 J mol^{-1} in this case. The austenite carbon concentration, calculated under CCEθ conditions using the cementite free energy taking the Si partitioning effect discussed above into account, is drawn in Fig. 13 as a green line (CCEθ-II). The calculated value is indeed much closer to the experimental data compared with the purple line, assuming para-cementite (i.e. without Si partitioning). If one assumes that Si is completely ejected from the cementite, the cementite free energy is even lower than that in the case of CCEθ-II. The austenite carbon concentration in this case was calculated as 1.7 wt.% under CCEθ conditions. This value is quite close to the experimentally observed austenite carbon concentration range, as shown in Fig. 13. Thus, the free energy of cementite has a significant influence on the austenite carbon concentration under CCEθ conditions. Therefore, partitioning of Si and Mn between ferrite and cementite should also be taken into account for a more accurate prediction of the austenite carbon concentration after a partitioning step in the case where cementite precipitation occurs inside the martensite. In many cases, carbide first precipitates in the form of transition carbides such as epsilon carbide and then transforms into cementite accompanied by the partitioning of substitutional elements [31]. It is therefore necessary to consider the free energy change in the corresponding carbides at each partitioning time step to predict the austenite carbon concentration accurately. The free energies of cementite as well as of epsilon carbide in multi-component systems are not yet fully understood and first-principles studies are being pursued along these lines [32,34].

In addition to the above discussion, the volume fraction of cementite can also be predicted to change with the martensite volume fraction according to the CCEθ model. Fig. 15 shows the volume fraction of cementite inside the martensite region for steel A (1.07 wt.% C) calculated by the CCEθ model as a function of the martensite volume fraction. The austenite carbon concentration after partitioning is assumed to be 1.1–1.3 wt.%. In the case of 1.2 wt.% C in austenite, which is the average experimental value observed in this study, the cementite fraction is predicted to decrease drastically when the martensite volume fraction is <20%. As mentioned in Section 3.1, the carbide number density in the specimen with 15 vol.% martensite (Fig. 4c, d) seems to be slightly lower compared with that in the specimens with higher martensite volume fraction (Fig. 4e–h). This trend is consistent with the prediction by the CCEθ model. However, the difference in carbide volume fraction between the specimen with 15 vol.% martensite (Fig. 4c, d) and that with 75 vol.% martensite (Fig. 4g, h) seems to be not as large compared with the prediction shown in Fig. 15. This can probably be attributed to the fact that the carbon partitioning did not reach the equilibrium state at 400 °C after 300 s as probed in this study (Fig. 7). It is likely that the carbide volume fraction decreases with ongoing heat treatment, although the equilibrium austenite carbon concentration decreases accompanied by the decrement of the carbide free energy during the partitioning step, which increases the carbide fraction (see comparison between 1.2 wt.% C and 1.1 wt.% C in Fig. 15). The volume fraction of carbide is predicted to be zero when the martensite volume fraction is lower than the critical values (e.g. ~11% for the case of 1.2 wt.% C in austenite). Therefore, if an accurate value for the carbide free energy is available, it is considered that the maximum limit of the martensite volume fraction to avoid carbide precipitation in martensite can be predicted. This situation corresponds to the upper limit boundary conditions assumed by the CCE model. Therefore, the transition from the CCE model (without carbide) to the CCEθ model (with carbide) can also be captured by the CCEθ model, which is considered to have a substantial effect on the mechanical properties.

5. Conclusions

The carbon partitioning behavior from martensite into austenite during a partitioning step accompanied by the carbide precipitation inside the martensite was investigated

by means of FE-EPMA and APT using 1.07 wt.% and 0.59 wt.% carbon steels with various martensite volume fractions. Carbon partitioning from martensite into austenite was clearly observed in both steels, even though considerable carbide precipitation was observed inside the martensite. The austenite carbon concentration after the partitioning step was not influenced by either the martensite volume fraction or the bulk carbon content. A modified prediction model for the austenite carbon concentration after the partitioning step in the Q&P process, which can be applied to the case where carbide precipitation occurs in martensite, was proposed to explain the experimental results. The austenite carbon concentration predicted by the modified model showed the same trend as the experimental results, i.e. it was independent of the martensite volume fraction and of the bulk carbon content. The predicted carbon value was closer to the experimental value than that predicted by the original CCE model. The predicted value was significantly influenced by the partitioning of substitutional elements between ferrite and carbide. Further studies are needed to take into account the kinetics of the free energy changes of carbide during the partitioning step for a more accurate prediction of austenite carbon concentration at each partitioning time step.

Acknowledgements

P. Choi and M. Herbig, Max-Planck-Institut für Eisenforschung GmbH, are gratefully acknowledged for helpful discussions on the APT data.

References

[1] J.G. Speer, A.M. Streicher, D.K. Matlock, F.C. Rizzo, G. Krauss, in: E.B. Damm, M. Merwin (Eds.), Austenite Formation and Decomposition, Warrendale, PA, TMS/ISS, 2003, p. 505.
[2] J.G. Speer, D.K. Matlock, D.V. Edmonds, Mater. Res. 8 (2005) 417.
[3] B.C. De Cooman, J.G. Speer, Steel Res. Int. 77 (2006) 634.
[4] E. De Moor, J.G. Speer, D.K. Matlock, J.H. Kwak, S.B. Lee, Steel Res. Int. 83 (2012) 322.
[5] J.G. Speer, D.K. Matlock, B.C. De Cooman, J.G. Schroth, Acta Mater. 51 (2003) 2611.
[6] M.J. Santofimia, L. Zhao, J. Sietsma, Metall. Mater. Trans. A 40A (2009) 46.
[7] D.V. Edmonds, K. He, F.C. Rizzo, B.C. De Cooman, D.K. Matlock, J.G. Speer, Mater. Sci. Eng., A 438–440 (2006) 25.
[8] Y. Toji, H. Matsuda, M. Herbig, P.-P. Choi, D. Raabe, Acta Mater. 65 (2014) 215.
[9] H.K.D.H. Bhadeshia, D.V. Edmonds, Metall. Trans. A 10A (1979) 895.
[10] M.J. Santofimia, T. Nguyen-Minh, L. Zhao, R. Petrov, I. Sabirov, J. Sietsma, Mater. Sci. Eng., A 527 (2010) 6429.
[11] Z.Q. Liu, G. Miyamoto, Z.G. Yang, T. Furuhara, Acta Mater. 61 (2013) 3120.
[12] A. Cerezo, T.J. Godfrey, G.D.W. Smith, Rev. Sci. Instrum. 59 (1988) 862.
[13] D. Blavette, B. Deconihout, A. Bostel, J.M. Sarrau, M. Bouet, A. Menand, Rev. Sci. Instrum. 64 (1993) 2911.
[14] M.K. Miller, A. Cerezo, M.G. Hetherington, G.D.W. Smith, Atom Probe Field Ion Microscopy, Oxford University Press, Oxford, 1996.
[15] K. Hono, Acta Mater. 47 (1999) 3127.
[16] M.K. Miller, Atom Probe Tomography Analysis at the Atomic Scale, Kluwer Academic/Plenum, New York, 2000.
[17] T.F. Kelly, M.K. Miller, Rev. Sci. Instrum. 78 (2007) 031101.
[18] P. Choi, M. da Silva, U. Klement, T. Al-Kassab, R. Kirchheim, Acta Mater. 53 (2005) 4473.
[19] E.A. Marquis, P. Choi, F. Danoix, K. Kruska, S. Lozano-Perez, D. Ponge, et al., Microsc. Today 20 (2012) 44.
[20] M.J. Duarte, J. Klemm, S.O. Klemm, K.J.J. Mayrhofer, M. Stratmann, S. Borodin, et al., Science 341 (2013) 372.
[21] M. Herbig, D. Raabe, Y.J. Li, P. Choi, S. Zaefferer, S. Goto, Phys. Rev. Lett. 112 (2014) 126103.
[22] K. Thompson, J. Sebastian, S. Gerstl, Ultramicroscopy 107 (2007) 124.
[23] Y.J. Li, P. Choi, C. Borchers, S. Westerkamp, S. Goto, D. Raabe, Acta Mater. 59 (2011) 3965.
[24] Y.J. Li, P. Choi, S. Goto, C. Borchers, D. Raabe, R. Kirchheim, Acta Mater. 60 (2012) 4005.
[25] M.G.H. Wells, Acta Metall. 12 (1964) 389.
[26] H.K.D.H. Bhadeshia, Acta Metall. 29 (1981) 1117.
[27] M.J. Santofimia, J.G. Speer, A.J. Clarke, L. Zhao, J. Sietsma, Acta Mater. 57 (2009) 4548.
[28] N.J. Petch, J. Iron Steel Inst. 149 (1944) 143.
[29] L. Battezzati, M. Baricco, S. Curiotto, Acta Mater. 53 (2005) 1849.
[30] G.A. Nematollahi, J. Von Pezold, J. Neugebauer, D. Raabe, Acta Mater. 61 (2013) 1773.
[31] G. Miyamoto, J.C. Oh, K. Hono, T. Furuhara, T. Maki, Acta Mater. 55 (2007) 5027.
[32] K.C. Ande, M.H.F. Sluiter, Acta Mater. 58 (2010) 6276.
[33] O.C. Hellman, J.A. Vandenbroucke, J. Rusing, D. Isheim, D.N. Seidman, Microsc. Microanal. 6 (2000) 437.
[34] B. Hallstedt, D. Djurovic, J. Appen, R. Dronskowski, A. Dick, F. Körmann, T. Hickel, J. Neugebauer, CALPHAD 34 (2010) 129.